Experimental analysis of flow birefringence in Jeffery-Hamel flow

M. Kobayashi[1,*], William. K.A. Worby[2], Y. Yokoyama[3], M. Kawaguchi[2], Y. Tagawa[2,**]

1: Dept. of Ind. Tech. and Innov., Tokyo University of Agriculture and Technology, Japan
2: Dept. of Mech. Sys. Eng., Tokyo University of Agriculture and Technology, Japan
3: Micro/Bio/Nanofluidics Unit, The Okinawa Institute of Science and Technology, Japan
Corresponding author, *:s242347u@st.go.tuat.ac.jp, **:tagawayo@cc.tuat.ac.jp

Keywords: Photoelaticity, Jeffery-Hamel flow, Particle alignment, Extensional-shear flow, High-speed polarization camera

ABSTRACT

Cardiovascular diseases are the leading cause of death globally, taking an estimated 20.5 million lives each year (Lindstrom et al., 2022). The onset and progression of these diseases are closely related to the stress distribution caused by blood flow within the vascular system. The mechanisms involved are still not fully understood, and non-invasive measurements of unsteady stress fields are required to gain a better understanding. Although stress estimation through simulations has been attempted, experimental validation to assess mathematical validity has not been conducted. The photoelastic method developed in solid mechanics is a non-contact, non-stationary stress field measurement method. The photoelastic method is being considered for application to fluids. In previous studies, simple shear flow and uniaxial extensional flow experiments have shown a relationship between the measured phase retardation and the velocity field. However, no clear relationship exists for extensional and shear combined flow fields. The objective of the present study is to clarify the relationship between the velocity field and the measured phase retardation in an extensional-shear combined flow. For this objective, photoelastic measurements were conducted in a steady flow field using the Jeffery-Hamel flow, which is an extensional-shear combined flow with an analytical solution for the velocity field. Comparison with the analytical velocity field showed that birefringence was proportional to the 0.88 and 0.92 power of the deformation in the shear or extensional-dominated region, respectively. The results show that the birefringence followed the power law of extensional rate $\dot{\varepsilon}$ ($\Delta_n \propto \dot{\varepsilon}^{0.95}$) where $\dot{\varepsilon}$ is dominant. Whereas shear is dominant, $\Delta_n \propto \dot{\gamma}^{0.88}$ holds. These results are consistent with previous studies using shear flow and uniaxial extensional flow. Furthermore, it is shown that in the extensional-shear combined flow, the sum-of-squares root of two equations, one of which is $\Delta_n = \dot{\gamma}^{0.88} \cdot 9.0 \times 10^{-8}$ where the shear rate dominates and the other of which is $\Delta_n = \dot{\varepsilon}^{0.95} \cdot 9.2 \times 10^{-8}$ in the region where the extensional rate dominates, holds. This suggests that the theory developed mainly for solids could also be applied to fluids.

1. Introduction

Since the wall stress distribution in blood vessels due to blood flow is closely related to the onset and progression of cardiovascular diseases, it is necessary to know the stress field. An example

of a disease is the rupture of a cerebral aneurysm. It has been reported that the rupture of cerebral aneurysms is caused in part by strong shear stress applied to the vessel wall (Shojima et al., 2004). The principle of cerebral aneurysm expansion, the rupture mechanism, and the progression mechanism of arteriosclerosis are not yet clear, and it is necessary to obtain stress distributions to elucidate them. Stress estimation by simulation has been carried out, however experimental validation to assess the validity of the mathematical models used is insufficient (Jansen et al., 2014). However, these methods are difficult to measure precisely in the near vicinity of the vessel wall and have limited spatio-temporal resolution. If a stress field measurement method can be developed to solve these problems, enabling quantitative stress measurement and identification of stress concentration points, it will lead to an elucidation of the mechanism. It is also expected that a treatment method and an imaging diagnosis method will be established that enables early detection. The development of a non-invasive stress field measurement method for unsteady and complex flow fields is therefore required. Hence, we have focused our attention on photoelastic measurements (Yokoyama et al., 2023; Worby et al., 2024; Nakamine et al., 2024). Photoelastic measurement has been developed in solid mechanics and is a method for non-invasively measuring unsteady stress fields. Adapting this method to fluids has the potential to be a better measurement technique than the methods described above.

The photoelastic method is a technique for measuring the stresses applied to an object by measuring the polarization state of transmitted light. The phase retardation and azimuth of the observed light correspond to the principal stress difference and the direction of the principal stress, respectively. To apply this method to fluid stress measurement, optically anisotropic particles are dispersed in the fluid. To establish photoelastic methods in fluids, studies have been carried out using different particles and measuring channels (Sato, 2022). Various flow channels have been studied, with measurements in shear flow fields using rectangular tubes and rheometers, and in extensional flow fields using Capillary Breakup Extensional Rheometry Dripping-onto-Substrate and Optimized Shape Cross-Slot Extensional Rheometer flow channels (Sharma et al., 2015; Muto & Tagawa, 2022).

In recent years, the photoelastic method was applied to the flow field by dispersing non-spherical particles in a solution (Schmidt et al., 2002). The flow aligns the particles, which leads to optical anisotropy in the fluid. Calabrese et al. (2021) conducted experiments in both extensional and shear flow, confirming that the retardation is expressed as a power of shear rate $\dot{\gamma}$ in shear flow and the extensional rate $\dot{\varepsilon}$ in uniaxial extensional flow. They provided the relationship $\Delta n \propto |\dot{\gamma}|^{0.9} \propto |4\dot{\varepsilon}|^{0.9}$. Lane et al. (2022) using a Taylor-Couette flow, showed the relationship between shear rate and birefringence as $\Delta n \propto |\dot{\gamma}|^{0.537}$. The different power exponents are believed to result from variations in particle interactions due to differences in the concentration of the photoelastic material, Cellulose nanocrystal (CNC) suspension, and differences in the length of CNC, lead to different rotational diffusion coefficients (Maguire et al., 1980). From both sets of results, it is evident that there is a power-law relationship between birefringence Δ_n and $\dot{\gamma}$, $\dot{\varepsilon}$. Previous studies

revealed the relationship between $\dot{\gamma}$ or $\dot{\varepsilon}$ and Δ_n in uniaxial extensional and shear flows. However, it has not been confirmed whether these relationships hold in the extensional-shear combined flows. Therefore, this study aims to use two-dimensional extensional-shear combined flow, Jeffery-Hamel flow, to elucidate the relationship between strain rate and Δ_n. This paper presents the results comparing them with the theoretical velocity field.

2. Jeffery-Hamel flow

The Jeffery-Hamel flow is illustrated in Fig. 1. The flow is a two-dimensional radial flow with a constant angle of the wall surface and the origin O serving as the source or sink. Considering polar coordinates as shown in Fig. 1, α [rad] is the angle of the flow channel wall surface with respect to the central axis. The distance (radius) from the origin O is denoted as r [m], and the velocity at an angle θ [rad] from the central axis is denoted as u_r [m/s]. The flow is perfectly radial, and the velocity component u_θ in the θ direction is 0, in the polar coordinate system, the continuity equation is expressed by

$$\frac{1}{r}\frac{\partial}{\partial r}\left(ru_r\right) = 0, \tag{1}$$

and the momentum conservation equations are represented by

$$u_r\frac{\partial u_r}{\partial r} = -\frac{1}{\rho}\frac{\partial p}{\partial r} + \nu\left(\frac{\partial^2 u_r}{\partial r^2} + \frac{1}{r}\frac{\partial u_r}{\partial r} - \frac{u_r}{r^2} + \frac{1}{r^2}\frac{\partial^2 u_r}{\partial \theta^2}\right), \tag{2}$$

$$0 = -\frac{1}{\rho r}\frac{\partial p}{\partial \theta} + \frac{2\nu}{r^2}\frac{\partial u_r}{\partial \theta}. \tag{3}$$

Assume that the flow velocity at $\theta = 0$ is $u_{\max}$. Here, defining $\eta = \dfrac{\theta}{\alpha}$, $\dfrac{u_r}{u_{\max}} = f(\eta)$, $Re = u_{\max}\dfrac{r\alpha}{\nu}$, the following third-order nonlinear equation is derived (White, 2006)

$$f''' + 2Re\alpha f f' + 4\alpha^2 f' = 0. \tag{4}$$

The wall surface is in no-slip condition. Also, since the flow is $u_{\max}$ at $\theta = 0$ and is symmetric, the boundary conditions are determined as follows:

$$f(+1) = f(-1) = 0,\ f(0) = 1,\ f'(0) = 0. \tag{5}$$

Consider the cylindrical coordinate system (r, θ, z). The velocity gradient tensor $\nabla \mathbf{u}_{ij}$ is shown in the following equation:

$$\nabla \mathbf{u}_{ij} = \begin{bmatrix} \dfrac{\partial u_r}{\partial r} & \dfrac{1}{r}\dfrac{\partial u_r}{\partial \theta} - \dfrac{u_\theta}{r} & \dfrac{\partial u_r}{\partial z} \\ \dfrac{\partial u_\theta}{\partial r} & \dfrac{1}{r}\dfrac{\partial u_\theta}{\partial \theta} + \dfrac{u_r}{r} & \dfrac{\partial u_\theta}{\partial z} \\ \dfrac{\partial u_z}{\partial r} & \dfrac{1}{r}\dfrac{\partial u_z}{\partial \theta} & \dfrac{\partial u_z}{\partial z} \end{bmatrix}, \tag{6}$$

The deformation rate tensor $\mathbf{S}_{ij}$ is therefore

$$\mathbf{S}_{ij} = \begin{bmatrix} \dfrac{\partial u_r}{\partial r} & \dfrac{1}{2}\left(\dfrac{1}{r}\dfrac{\partial u_r}{\partial \theta} + \dfrac{\partial u_\theta}{\partial r} - \dfrac{u_\theta}{r}\right) & \dfrac{1}{2}\left(\dfrac{\partial u_r}{\partial z} + \dfrac{\partial u_z}{\partial r}\right) \\ \dfrac{1}{2}\left(\dfrac{1}{r}\dfrac{\partial u_r}{\partial \theta} + \dfrac{\partial u_\theta}{\partial r} - \dfrac{u_\theta}{r}\right) & \dfrac{1}{r}\dfrac{\partial u_\theta}{\partial \theta} + \dfrac{u_r}{r} & \dfrac{1}{2}\left(\dfrac{\partial u_\theta}{\partial z} + \dfrac{1}{r}\dfrac{\partial u_z}{\partial \theta}\right) \\ \dfrac{1}{2}\left(\dfrac{\partial u_r}{\partial z} + \dfrac{\partial u_z}{\partial r}\right) & \dfrac{1}{2}\left(\dfrac{\partial u_\theta}{\partial z} + \dfrac{1}{r}\dfrac{\partial u_z}{\partial \theta}\right) & \dfrac{\partial u_z}{\partial z} \end{bmatrix}. \tag{7}$$

If the pressure is p and the viscosity is μ, the stress tensor σ_{ij} is given by

$$\sigma_{ij} = \begin{bmatrix} -p + 2\mu\dfrac{\partial u_r}{\partial r} & \mu\left(\dfrac{1}{r}\dfrac{\partial u_r}{\partial \theta} + \dfrac{\partial u_\theta}{\partial r} - \dfrac{u_\theta}{r}\right) & \mu\left(\dfrac{\partial u_r}{\partial z} + \dfrac{\partial u_z}{\partial r}\right) \\ \mu\left(\dfrac{1}{r}\dfrac{\partial u_r}{\partial \theta} + \dfrac{\partial u_\theta}{\partial r} - \dfrac{u_\theta}{r}\right) & -p + 2\mu\left(\dfrac{1}{r}\dfrac{\partial u_\theta}{\partial \theta} + \dfrac{u_r}{r}\right) & \mu\left(\dfrac{\partial u_\theta}{\partial z} + \dfrac{1}{r}\dfrac{\partial u_z}{\partial \theta}\right) \\ \mu\left(\dfrac{\partial u_r}{\partial z} + \dfrac{\partial u_z}{\partial r}\right) & \mu\left(\dfrac{\partial u_\theta}{\partial z} + \dfrac{1}{r}\dfrac{\partial u_z}{\partial \theta}\right) & -p + 2\mu\dfrac{\partial u_z}{\partial z} \end{bmatrix}. \tag{8}$$

The velocity gradient tensor $\nabla \mathbf{u}_{ij}$, the deformation velocity tensor $\mathbf{S}_{ij}$ and the stress tensor σ_{ij} considering $u_\theta = 0, u_z = 0, \dfrac{\partial}{\partial z} = 0$ in a Jeffery-Hamel flow is shown in the following equations:

$$\nabla \mathbf{u}_{ij} = \begin{bmatrix} \dfrac{\partial u_r}{\partial r} & \dfrac{1}{r}\dfrac{\partial u_r}{\partial \theta} & 0 \\ 0 & \dfrac{u_r}{r} & 0 \\ 0 & 0 & 0 \end{bmatrix}, \tag{9}$$

$$\mathbf{S}_{ij} = \begin{bmatrix} \dfrac{\partial u_r}{\partial r} & \dfrac{1}{2r}\dfrac{\partial u_r}{\partial \theta} & 0 \\ \dfrac{1}{2r}\dfrac{\partial u_r}{\partial \theta} & \dfrac{u_r}{r} & 0 \\ 0 & 0 & 0 \end{bmatrix}. \tag{10}$$

$$\sigma_{ij} = \begin{bmatrix} -p + 2\mu\dfrac{\partial u_r}{\partial r} & \mu\left(\dfrac{1}{r}\dfrac{\partial u_r}{\partial \theta}\right) & 0 \\ \mu\left(\dfrac{1}{r}\dfrac{\partial u_r}{\partial \theta}\right) & -p + 2\mu\left(\dfrac{u_r}{r}\right) & 0 \\ 0 & 0 & 0 \end{bmatrix}. \tag{11}$$

The principal strain rate $\dot{\Gamma}$ (derived from the second invariant Π_S), shear rate $\dot{\gamma}$, and extensional

rate $\dot{\varepsilon}$ of the Jeffery-Hamel Flow are expressed as

$$\dot{\Gamma} = \sqrt{2\Pi_S} = \sqrt{2\left\{\left(\frac{\partial u_r}{\partial r}\right)^2 + \frac{1}{2}\left(\frac{1}{r}\frac{\partial u_r}{\partial \theta}\right)^2 + \left(\frac{u_r}{r}\right)^2\right\}}, \tag{12}$$

$$\dot{\gamma} = \frac{1}{r}\frac{\partial u_r}{\partial \theta}, \tag{13}$$

$$\dot{\varepsilon} = \frac{\partial u_r}{\partial r} - \frac{u_r}{r}. \tag{14}$$

The principal stress difference in the Jeffery-Hamel flow is shown in the following equation.

$$\begin{aligned}\sigma_{\text{sec}} &= \sqrt{(\sigma_{rr} - \sigma_{\theta\theta})^2 + 4\sigma_{r\theta}^2} \\ &= \sqrt{\left(2\mu\frac{\partial u_r}{\partial r} - 2\mu\frac{u_r}{r}\right)^2 + 4\left(\mu\left(\frac{1}{r}\frac{\partial u_r}{\partial \theta}\right)\right)^2} \\ &= 2\mu\sqrt{\left(\frac{\partial u_r}{\partial r} - \frac{u_r}{r}\right)^2 + \left(\frac{1}{r}\frac{\partial u_r}{\partial \theta}\right)^2},\end{aligned} \tag{15}$$

Transforming Eq. (15) using Eq. (13) and Eq. (14) leads as follows.

$$\sigma_{\text{sec}} = 2\mu\sqrt{\dot{\varepsilon}^2 + \dot{\gamma}^2}. \tag{16}$$

While extensional flow is dominant ($\dot{\gamma} \ll \dot{\varepsilon}$) near the channel center, shear flow is dominant near the channel wall ($\dot{\gamma} \gg \dot{\varepsilon}$).

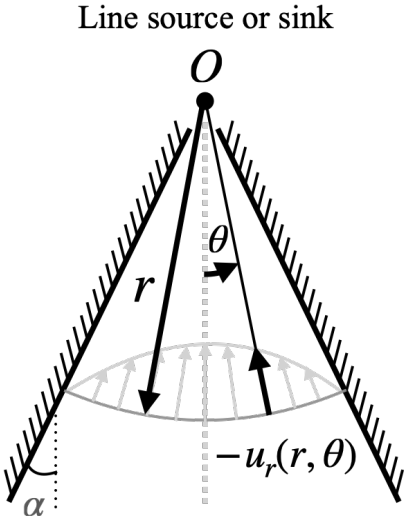

Figure 1. Jeffery-Hamel flow.

3. Photoelastic measurement

The photoelastic method (Aben et al., 2000) has developed as a technique for measuring stress fields in solids. When stress is applied to a photoelastic material, it exhibits the property of causing different refractive indices depending on the vibration direction of light, a phenomenon known as birefringence. The photoelastic method utilizes the phenomenon of birefringence, enabling non-contact stress field measurements. When circularly polarized light is incident to a stress-loaded photoelastic material, birefringence cause different phase retardation depending on the vibration direction of light, resulting in elliptically polarized light. Elliptically polarized light is characterized by two optical parameters, retardation Δ and orientation ϕ. The retardation Δ is associated with the secondary principal stress, while orientation ϕ is related to the direction of the principal stress. The relationship between the retardation Δ and the principal stress is expressed by the stress-optic law (*Photoelasticity of Glass*, 2012):

$$\Delta = Cd\sigma_{\mathrm{sec}}, \tag{17}$$

where C [1/Pa] is the photoelastic modulus, d [m] is the thickness of the measured object in the optical axis direction, and σ_{sec} [Pa] is mutually orthogonal principal stress differences. Note that Eq.(17) is valid only when the principal stress and the camera's optical axis direction are perpendicular, and the distribution of principal stress along the optical axis direction is constant. Here, birefringence Δ_n is defined as follows:

$$\Delta_n = \Delta/d. \tag{18}$$

The measurement principle of the photoelastic method is shown in Fig. 2. Circularly polarized light transforms into elliptically polarized light when transmitted to a fluid experiencing birefringence. The measurement principle of the polarized camera is depicted in Fig. 3. The high-speed polarization camera incorporates four polarizers in different directions ($0°$, $45°$, $90°$ and $135°$). The retardation of the incident light is calculated based on the light intensities of each polarizer (I_0, I_45, I_{90} and I_{135}) (Onuma & Otani, 2014) as follows:

$$\Delta = \frac{\lambda}{2\pi} \sin^{-1} \frac{\sqrt{(I_{90} - I_0)^2 + (I_{45} - I_{135})^2}}{(I_0 + I_{45} + I_{90} + I_{135})/2}. \tag{19}$$

where λ is the wavelength of the light source.

4. Experimental method

Figure 4 shows the schematic of the experimental setup. The channel is positioned between the light source and the high-speed polarization camera (CRYSTA PI-5WP, Photoron Co., Ltd, flame

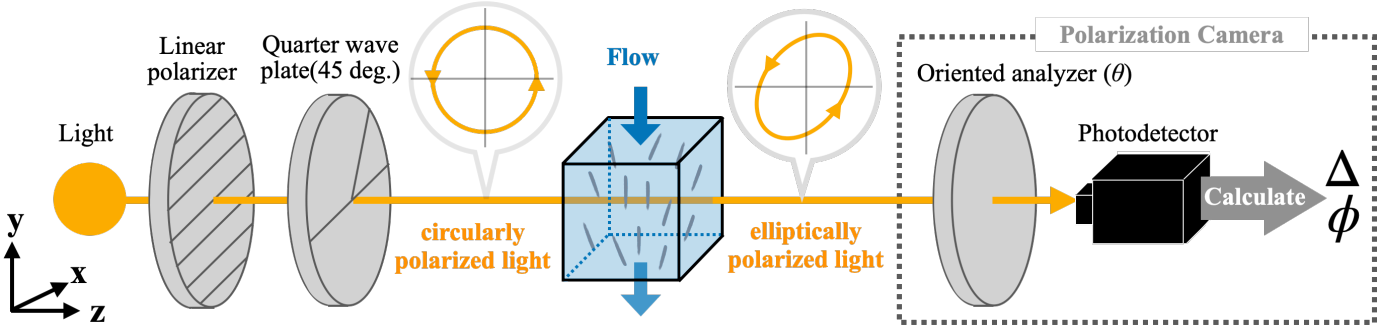

Figure 2. Illustration of a photoelastic method.

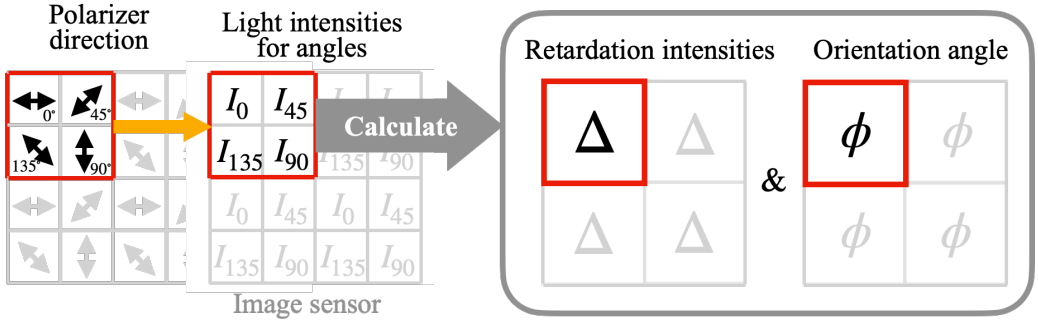

Figure 3. Schematic diagram of the measurement principle and image sensors of a high-speed polarization camera. The four polarization sensors acquire the polarization intensity and calculate the retardation Δ and the orientation angle ϕ. The direction of the polarizers shown in the diagram indicates the direction of oscillation of the light transitting.

rate: 250 f.p.s.). The channel was fabricated using a 3D printer. The channel has a shape that includes an entrance region before and after the Jeffery-Hamel flow section. It features a wall angle of $\alpha = 15°$, a narrow part of 1 mm, and a depth of $d = 25$ mm.

The working fluid was CNC (CNC-HS-FD, Cellulose Lab Co. Ltd.) mixed suspension. CNCs are rod-like nanoparticles, which exhibit birefringence by orienting in the corresponding direction to stress. CNC was dispersed in ultra-pure water and stirred for more than two hours at $25°$C using a stirrer (CHPS-170DF, ASONE Co., Ltd.) rotating at 600 rpm. The concentration of CNC suspension was set to 1.0 wt %. The CNC suspension is then sonicated using a homogenizer (UX-300, Mitsui Electric Co. Ltd.) for 200 seconds (total working time:10 min (OFF time: 20 s, ON time: 10 s)) to disperse the individual CNC nanorods.

Figure 5 shows the shear viscosity of CNC suspension measured by a cone-plate type rheometer (MCR302, Anton Paar) at $22°$C. The data represent the averaged values obtained from four individual measurements. In this paper, we approximated CNC suspension as a Newtonian fluid. The flow rate was controlled by a syringe pump (PUMP 11 ELITE, Harvard Apparatus) in the range of 10 – 50 ml/min at intervals of 10 ml/min. The flow direction was in the narrowing direction

(opposite to gravity). After a steady state was reached, the flow field was recorded for two seconds using a high-speed polarization camera (250 fps, 500 frames).

The obtained light intensity values were binarized to detect the channel walls. Then, we determined the coordinates of the hypothetical sink's origin in the Jeffery-Hamel flow.

As the measurements were conducted in a steady state, we used time-averaged Δ_n measurements for analysis. Both analytical and experimental results were compared using polar coordinates, as shown in Fig. 1. In addition, to mitigate the left-right asymmetry in the retardation distribution caused by a slight elliptical polarization of the light source, we used the averaged values at points where $|\theta|$ is the same.

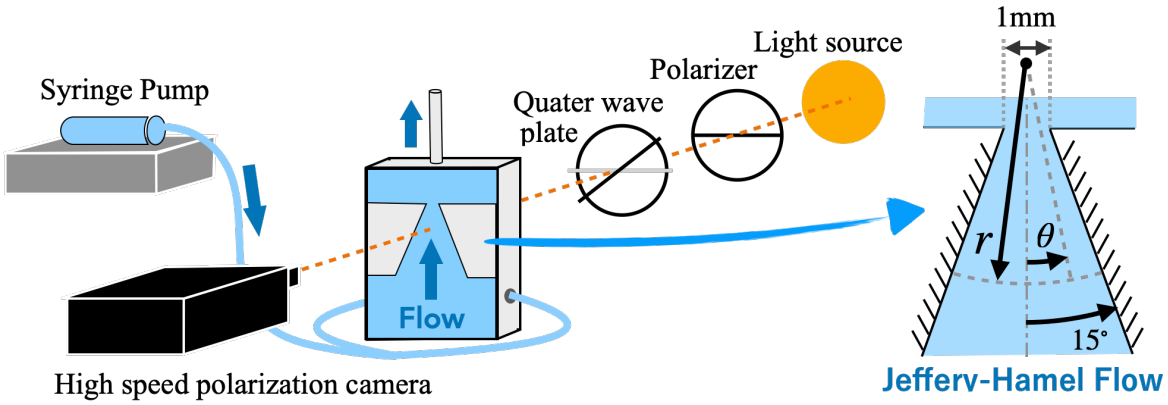

Figure 4. A schematic of the experimental setup.

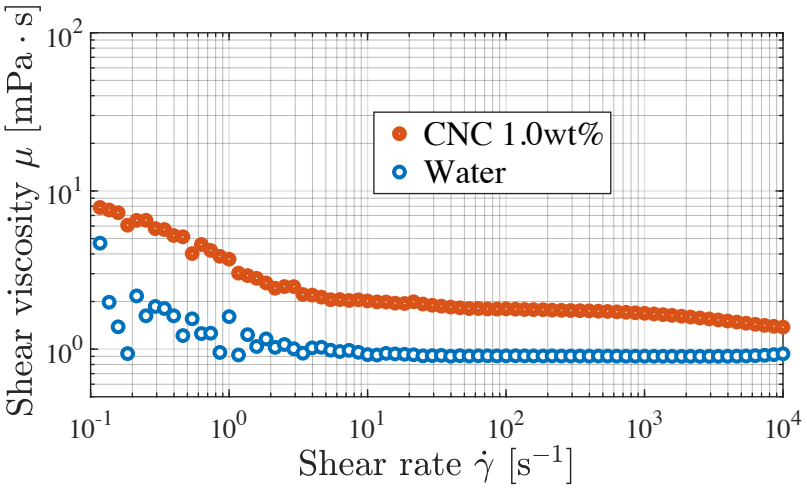

Figure 5. Shear viscosity μ versus shear rate $\dot{\gamma}$.

5. Results and discussion

Figure 6 shows the visualized image of the birefringence field with a scale of 29 pixels/mm. The values on the channel walls have been replaced with zeros. In Fig. 6, focusing on the θ direction, the birefringence value increases from $\theta = 0$ (center of the channel) to $\theta = \alpha$ (channel wall). In addition, focusing on the r direction, the birefringence value increases as r decreases. It indicates that birefringence increases at higher shear rates. In previous studies, it has been shown that the birefringence increases as the shear rate or extensional rate increases (Calabrese et al., 2021; Lane et al., 2022; Worby et al., 2024). Qualitative considerations show that the results of this experiment follow the same trend as in previous studies.

To compare with previous studies that utilize a different coordinate system, we introduced invariants. First, we compare measured birefringence Δ_n with the invariant derived from the analytical solution of the velocity field, the principal strain rate $\dot{\Gamma}$. We extracted results from the circular arc at $r = 3.0\ \mathrm{mm}$. Figure 7 shows the birefringence versus principal strain rate results. The color represents the difference in flow rate during the experiment. For each flow rate condition, the principal strain rate becomes larger along the arc and it reaches the maximum value at the wall. The results shown in Fig. 7 indicate that Δ_n is proportional to the 0.88 power of the principal strain rate ($\Delta_n \propto \dot{\Gamma}^{0.88}$). This result agrees with previous studies regarding a power-law dependence on the velocity gradient. The power exponent derived in the present study was 0.88, which lies between exponents of 0.537 (Lane et al., 2022) and that of 0.9 (Calabrese et al., 2021). This could be due to differences in the concentration of the suspension and the length of the CNC. The concentration of the CNC suspension in this experiment was 1.0 wt%. The length of the CNC used is 250 nm. In addition, since Jeffery-Hamel flow represents a flow field with only radial velocities, further investigation is needed to confirm whether the proportional relationship with the power of the principal strain rate holds in the extensional-shear combined flows with different flow channel geometries.

Figure 8 shows the relationship between birefringence Δ_n and the ratio of extensional rate to shear rate $\dot{\gamma}/\dot{\varepsilon}$, where results on the arc with $r = 3.0\ \mathrm{mm}$. Δ_n was obtained from polarization measurements and $\dot{\gamma}/\dot{\varepsilon}$ was calculated from the analytical solution of the velocity field. Smaller values of $\dot{\gamma}/\dot{\varepsilon}$ indicate that the extensional rate is dominant, while larger values of $\dot{\gamma}/\dot{\varepsilon}$ indicate that the shear rate is dominant. At its lowest and highest points, the value was approximated as being only the extensional rate or the shear rate and fitted with a power of $\dot{\varepsilon}$ or $\dot{\gamma}$. As a result, a relationship of $\Delta_n = \dot{\varepsilon}^{0.95} \cdot 9.2 \times 10^{-8}$ was obtained in the region where the extensional rate is dominant. On the other hand, the relationship $\Delta_n = \dot{\gamma}^{0.88} \cdot 9.0 \times 10^{-8}$ was obtained in the region where the shear rate is dominant. From Fig. 8, in the region where $\dot{\gamma}/\dot{\varepsilon} < 10^{-1}$, the measurement results align well with $\Delta_n \propto \dot{\varepsilon}^{0.95}$, and in the region where $\dot{\gamma}/\dot{\varepsilon} > 10^{1}$, the measurement results align well with $\Delta_n \propto \dot{\gamma}^{0.88}$.

Next, we focused on the relationship between Δ_n, $\dot{\varepsilon}$ and $\dot{\gamma}$ in the extensional-shear combined region of $10^{-1} < \dot{\gamma}/\dot{\varepsilon} < 10^{1}$. This area has not been experimentally investigated. So far thus, as shown in

Eq. (17), the stress-optic law $\Delta_n = C\sigma_{\mathrm{sec}}$, used in solid mechanics, was introduced. The principal stress difference σ_{sec} can be expressed as $\sigma_{\mathrm{sec}} = 2\mu\sqrt{\dot{\varepsilon}^2 + \dot{\gamma}^2}$ in the Jeffery-Hamel flow, as shown in Eqs. (15) and (16). By replacing $\dot{\varepsilon}$ and $\dot{\gamma}$ in the equation for $\sigma_{\mathrm{sec}} = 2\mu\sqrt{\dot{\varepsilon}^2 + \dot{\gamma}^2}$ (Eq. (16)) by $\dot{\varepsilon}^{0.95} \cdot 9.2 \times 10^{-8}$ and $\dot{\gamma}^{0.88} \cdot 9.0 \times 10^{-8}$ obtained by fitting the experimental values, we obtained $\sqrt{(\dot{\varepsilon}^{0.95} \cdot 9.2 \times 10^{-8})^2 + (\dot{\gamma}^{0.88} \cdot 9.0 \times 10^{-8})^2}$. This equation is shown by the solid line in Fig. 8. The results shown in Fig. 8 indicate that the experimental results showed good agreement with the practice using the concept of principal stress difference. For shear and extensional flows, the only comparison with the theory presented in Fig. 8 was the measurement results at $r = 3.0\ \mathrm{mm}$, but if it can be confirmed that this relationship holds for other conditions, it may be possible to identify a universal relationship that holds for the extensional-shear combined flows.

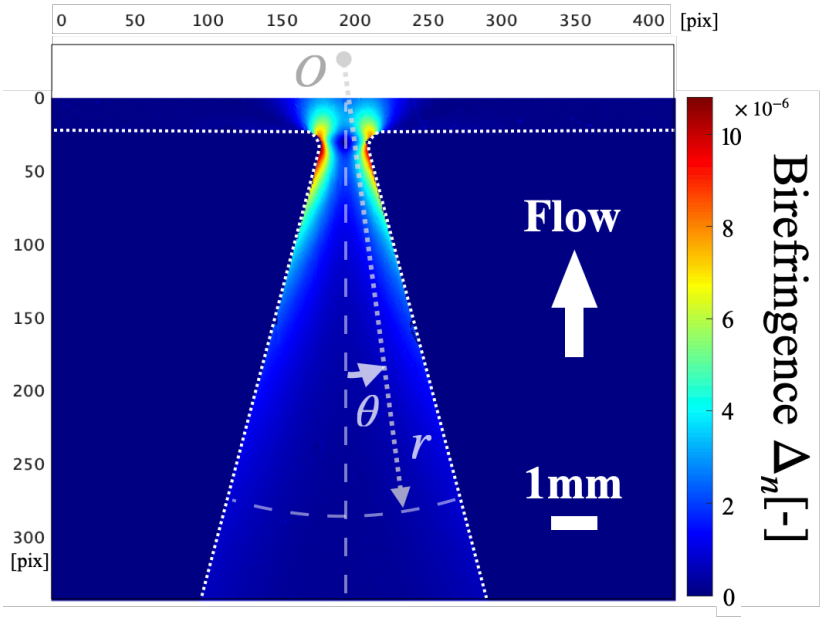

Figure 6. Birefringence measurement value of CNC suspension at the flow rate of $30\ \mathrm{ml/min}$, showing time-averaged values taken at 250 fps for 2 s. The contour plot displays the birefringence Δ_n. The white dashed lines indicate the channel walls.

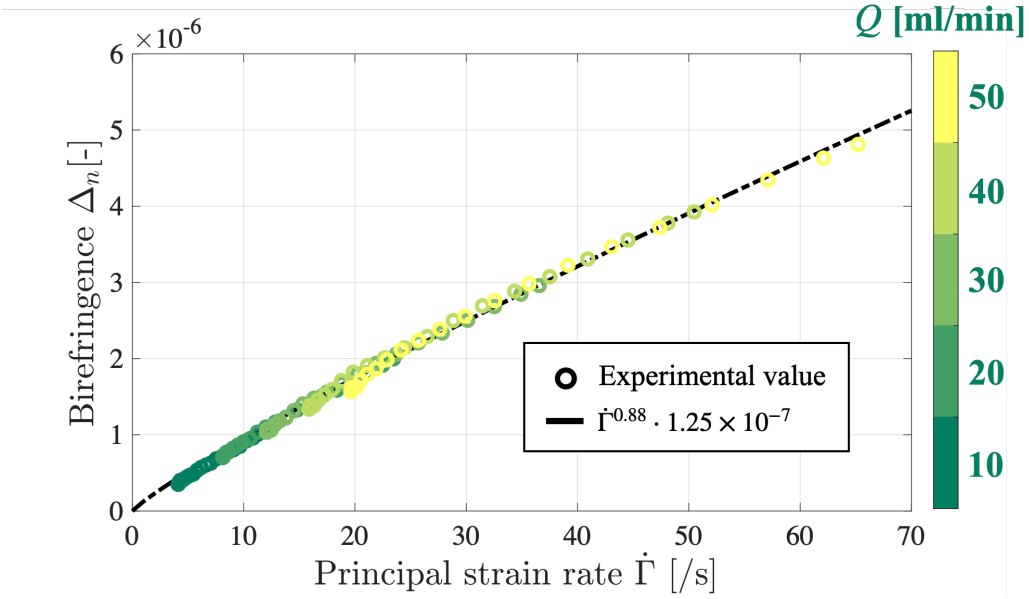

Figure 7. Birefringence Δ_n versus the principal strain rate $\dot{\Gamma}$ derived from the velocity field of the analytical solution. The plots are experimental results and their colors correspond to flow rates.

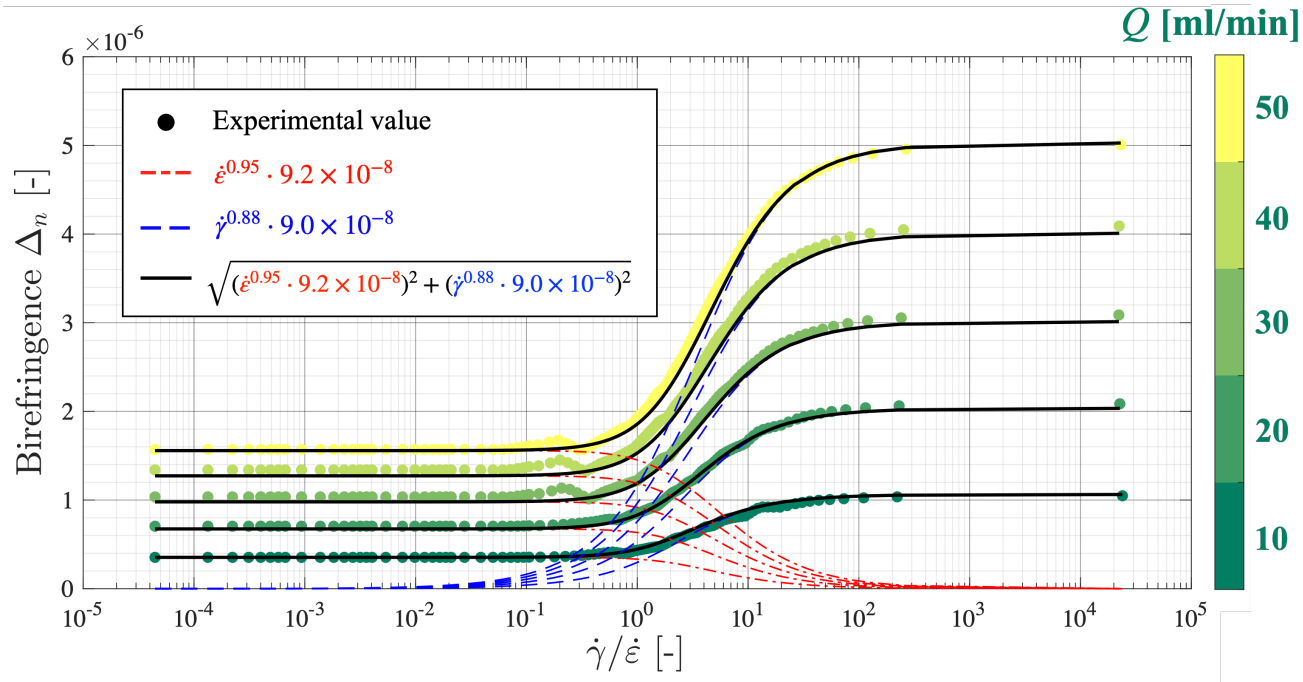

Figure 8. Relationship between measured birefringence Δ_n and the ratio of shear and extensional rate $\dot{\gamma}/\dot{\varepsilon}$ obtained from analytical solution. The plots are experimental results and the colors correspond to flow rates. The dashed line is power law trends as $\Delta_n \propto \dot{\varepsilon}^{0.95}$, and the dotted line is power law trends as $\Delta_n \propto \dot{\gamma}^{0.88}$. The solid line is the sum-of-squares root of the two equations.

6. Conclusion

This study aimed to clarify the relationship between photoelastic measurements and velocity fields in extensional-shear combined flows. For this purpose, steady flow field polarization measurements were conducted using the Jeffery-Hamel flow, which is the extensional-shear combined flow and a flow field where an analytical solution for the velocity field exists. The polarisation parameter Δ was measured with a high-speed polarisation camera and converted to Δ_n. The velocity field was calculated numerically. The relationship between the time-averaged Δ_n and the extensional, shear, and strain rates calculated from the velocity field was investigated. The results showed that $\Delta_n \propto \dot{\varepsilon}^{0.95}$ was established in the region where the extensional rate was dominant, while $\Delta_n \propto \dot{\gamma}^{0.88}$ was established in the region where the shear rate was dominant. The results are in agreement with previous studies using shear-only and uniaxial extensional-only flow channels. A power-law relationship between phase retardation and shear rate and between phase retardation and extensional rate is shown. In addition, in the region where there are both shear and extensional flow, the sum-of-squares root of the two equations, $\sqrt{(\dot{\varepsilon}^{0.95} \cdot 9.2 \times 10^{-8})^2 + (\dot{\gamma}^{0.88} \cdot 9.0 \times 10^{-8})^2}$, showed good agreement with Δ_n. This can be explained by the stress optic law in solids. Future discussions will also involve considerations of orientation, exploring how particle alignment corresponds to velocity distributions.

Acknowledgements

This work was supported by JSPS KAKENHI Grant No. JP20H00223, and JST PRESTO Grant No. JPMJPR21O5. The authors thank Dr. Connor Lane and Prof. Thomas Rösgen from ETH Zürich for sharing his flow channel with us.

References

Aben, H., Ainola, L., & Anton, J. (2000). Integrated photoelasticity for nondestructive residual stress measurement in glass. *Optics and Lasers in Engineering*, *33*(1), 49–64.

Calabrese, V., Haward, S. J., & Shen, A. Q. (2021). Effects of Shearing and Extensional Flows on the Alignment of Colloidal Rods. *Macromolecules*, *54*(9), 4176–4185.

Jansen, I., Schneiders, J., Potters, W., van Ooij, P., van den Berg, R., van Bavel, E., … Majoie, C. (2014). Generalized versus patient-specific inflow boundary conditions in computational fluid dynamics simulations of cerebral aneurysmal hemodynamics. *American Journal of Neuroradiology*, *35*(8), 1543–1548.

Lane, C., Rode, D., & Rösgen, T. (2022). Birefringent properties of aqueous cellulose nanocrystal suspensions. *Cellulose*, *29*(11), 6093–6107.

Lindstrom, M., DeCleene, N., Dorsey, H., Fuster, V., Johnson, C. O., LeGrand, K. E., … Roth, G. A. (2022). Global Burden of Cardiovascular Diseases and Risks Collaboration, 1990-2021. *Journal of the American College of Cardiology*, *80*(25), 2372–2425.

Maguire, J. F., McTague, J. P., & Rondelez, F. (1980). Rotational Diffusion of Sterically Interacting Rodlike Macromolecules. *Physical Review Letters*, *45*(23), 1891–1894.

Muto, M., & Tagawa, Y. (2022). *Unsteady rheo-optical measurements of uniaxially extending liquid polymers.* arXiv.

Nakamine, K., Yokoyama, Y., Worby, W. K. A., Muto, M., & Tagawa, Y. (2024). *Flow birefringence of cellulose nanocrystal suspensions in three-dimensional flow fields: Revisiting the stress-optic law.* arXiv.

Onuma, T., & Otani, Y. (2014). A development of two-dimensional birefringence distribution measurement system with a sampling rate of 1.3MHz. *Optics Communications*, *315*, 69–73.

Photoelasticity of Glass. (2012). Springer Berlin Heidelberg.

Sato, T. (2022). Experimental Studies of Flow-Induced Birefringence in Complex Fluids. *Journal of the Society of Rheology Japan*, *50*(1), 69–72.

Schmidt, G., Nakatani, A. I., & Han, C. C. (2002). Rheology and flow-birefringence from viscoelastic polymer-clay solutions. *Rheologica Acta*, *41*(1), 45–54.

Sharma, V., J. Haward, S., Serdy, J., Keshavarz, B., Soderlund, A., Threlfall-Holmes, P., & H. McKinley, G. (2015). The rheology of aqueous solutions of ethyl hydroxy-ethyl cellulose (EHEC) and its hydrophobically modified analogue (hmEHEC): Extensional flow response in capillary breakup, jetting (ROJER) and in a cross-slot extensional rheometer. *Soft Matter*, *11*(16), 3251–3270.

Shojima, M., Oshima, M., Takagi, K., Torii, R., Hayakawa, M., Katada, K., … Kirino, T. (2004). Magnitude and Role of Wall Shear Stress on Cerebral Aneurysm. *Stroke*, *35*(11), 2500–2505.

White, F. M. (2006). VISCOUS FLUID FLOW THIRD EDITION. *McGraw-Hill Inc.*.

Worby, W. K. A., Nakamine, K., Yokoyama, Y., Muto, M., & Tagawa, Y. (2024). *Examination of flow birefringence induced by the shear components along the optical axis using a parallel-plate-type rheometer.* arXiv.

Yokoyama, Y., Mitchell, B. R., Nassiri, A., Kinsey, B. L., Korkolis, Y. P., & Tagawa, Y. (2023). Integrated photoelasticity in a soft material: Phase retardation, azimuthal angle, and stress-optic coefficient. *Optics and Lasers in Engineering*, *161*, 107335.